Calculation of tensorial flow properties on pore level: Exploring the influence of boundary conditions on the permeability of three-dimensional stochastic reconstructions

Kirill M. Gerke [1,2,3,4,5,*] Marina V. Karsanina,[1,2] and Regina Katsman[6]

[1]*Schmidt Institute of Physics of the Earth of Russian Academy of Sciences, Moscow 107031, Russia*
[2]*Institute of Geospheres Dynamics of Russian Academy of Sciences, Moscow 119334, Russia*
[3]*Dokuchaev Soil Science Institute of Russian Academy of Sciences, Moscow 119017, Russia*
[4]*Kazan Federal University, Kazan 420008, Russia*
[5]*Moscow Institute of Physics and Technology, Dolgoprudny 141701, Russia*
[6]*Department of Marine Geosciences, Haifa University, Haifa 3498838, Israel*

While it is well known that permeability is a tensorial property, it is usually reported as a scalar property or only diagonal values are reported. However, experimental evaluation of tensorial flow properties is problematic. Pore-scale modeling using three-dimensional (3D) images of porous media with subsequent upscaling to a continuum scale (homogenization) is a valuable alternative. In this study, we explore the influence of different types of boundary conditions on the external walls of the representative modeling domain along the applied pressure gradient on the magnitude and orientation of the computed permeability tensor. To implement periodic flow boundary conditions, we utilized stochastic reconstruction methodology to create statistically similar (to real porous media structures) geometrically periodic 3D structures. Stochastic reconstructions are similar to encapsulation of the porous media into statistically similar geometrically periodic one with the same permeability tensor. Seven main boundary conditions (BC) were implemented: closed walls, periodic flow, slip on the walls, linear pressure, translation, symmetry, and immersion. The different combinations of BCs amounted to a total number of 15 BC variations. All these BCs significantly influenced the resulting tensorial permeabilities, including both magnitude and orientation. Periodic boundary conditions produced the most physical flow patterns, while other classical BCs either suppressed crucial transversal flows or resulted in unphysical currents. Our results are crucial to performing flow properties upscaling and will be relevant to computing not only single-phase but also multiphase flow properties. Moreover, other calculation of physical properties such as some mechanical, transport, or heat conduction properties may benefit from the technique described in this study.

I. INTRODUCTION

The exact description of pore-scale flow and transport is of great interest in numerous scientific and industrial fields: petroleum engineering [1,2], hydrology [3,4], soil science [5], fuel cell development [6], nuclear waste disposal [7,8], and food engineering [9], to name just a few. Such description is helpful in numerous instances, one of which is the possibility of supplying input data to larger-scale Darcian continuum models for potential future usage. Depending on the degree of anisotropy and statistical inhomogeneity of the modelled porous media domain, the introduction of tensorial flow properties into hydrodynamics simulators may significantly influence results [10–12], as only diagonal terms (i.e., flow properties derived from flow rate collinear with pressure gradient along three major orthogonal directions) are usually utilized for parametrization. However, the possibility to compute the full tensor of flow properties is especially attractive due to the increasing complexity of its measurements in the laboratory (e.g., Ref. [13]). Tensorial flow and transport properties may

include permeability, relative permeabilities, and capillary curves for two- and three-phase filtration, dispersion tensor for species transport, and other useful properties. While all of them are important in the aforementioned research fields, from now on we shall mainly focus on permeability due to the pervasiveness of the problem; also, permeability is crucial in the evaluation of all other properties (e.g., defines the absolute maximum for relative permeability curves or represents flow field necessary to simulate dispersion).

Although tensorial permeabilities were reported in research studies previously, the accuracy of the obtained solutions may be low due to the uncertainty with boundary conditions (BCs). In order to compute permeability tensor, one needs to simulate the velocity field, which is usually obtained using the lattice Boltzmann (LBM) method [14,15], finite-difference (FDM) Stokes solver [14,16], finite-element (FEM) or finite-volume method [17,18], or pore networks [19]. Each approach has some specific implementation of the boundary conditions, but in general, they utilize conventional options such as closed walls along imposed pressure gradient or periodic boundary conditions on these walls (within a rectangular or cubic modeling domain). As was recently discussed by Guibert *et al.* [18], such boundary conditions

*kg@ifz.ru

are not necessarily physically meaningful. They explored a number of additional, more physically based, boundary conditions (e.g., linear pressure or immersion into porous region of known properties) but limited their study to nonperiodic two-dimensional (2D) pore structures.

It is important to understand that implementation of boundary conditions for pore-scale simulations is generally affected by two different factors: (1) the principles of the numerical method utilized and its computational efficiency and (2) the way the 3D pore geometry images are obtained. In the case of the first factor, for example, the linear pressure boundary condition is not easy to impose in LBM and FDM models due to inherent numerical schemes; the periodic or symmetric configuration requires the enlargement of the modeling domain 8 times for 3D simulations, which is computationally expensive. The 3D images of porous media are usually obtained using x-ray computed tomography imaging [20–22] or combinations of methods to fuse multiscale images [23–25]. The resulting structure represents a limited volume of pores connected to pores outside the sample, which readily conduct flow if placed within porous media massif. But these pores are no longer interconnected if the sample is extracted from the surrounding media, and a simple application of periodic boundary conditions or copying with translation is not a relevant solution. This is due to the fact that real porous media images are rarely, if ever, periodic or symmetric. This explains why these conventional boundary conditions are not accurate, yet more physically meaningful conditions are nearly impossible to implement. To solve this problem, Guibert *et al.* [18] proposed a novel boundary condition that technically applies flow periodicity to nonperiodic structure by adding continuum homogeneous layers outside the pore-scale modeling domain and utilizing effective medium approximation. While nondiagonal values of the tensor obtained using this approach were naturally more symmetrical than for any other method they tested, the diagonal values were significantly lower. Moreover, the method involved Brinkmans model of coupling between continuum- and pore-scale domains and iterative solutions for simultaneous modeling in both of them, which requires additional meshing and computational effort.

Our study was inspired by the stimulating work of Guibert *et al.* [18] and the idea that permeability tensor computed on 3D periodic geometries applying periodic flow conditions can be a relevant approach. There is a method to produce 3D images based on limited input data called stochastic reconstruction. Originally the idea of this approach was to create 3D structure from its 2D representation when x-ray microtomography devices were not yet available for extensive usage [26,27], but later it was recognized that stochastic reconstruction can be useful in many other instances [28–32], including building multiscale structure digital models [25,33–35] or characterizing subsurface geological domains via multiple-point statistics [36,37]. Regardless of the exact methodology employed, if during reconstruction geometrical periodic boundary is applied, it is possible to create a statistically similar replica of the original porous media where any pore leaving one boundary of the domain will reconnect to the pore on the other side. The objective of this paper is to explore the influence of boundary conditions on pore-scale simulated permeability tensor. But unlike previous works, here we

utilized stochastic reconstructions to create statistically similar replicas of real pore geometries with periodic pore structures. This idea establishes a new approach to assess tensorial flow properties based on stochastic reconstructions with simple, yet physically meaningful, flow modeling boundary conditions.

II. MATERIALS AND METHODS

A. Three-dimensional pore geometries

To create stochastic replicas, we chose two porous media of different genesis—shale and soil samples. Original images are 2D slices obtained using x-ray microtomography [38] and thin sectioning [30], respectively. These already-segmented (separated into pores and solids) images were rotated to redirect the major anisotropy in a diagonal direction (to increase the magnitude of the off-diagonal terms of the computed permeability tensors) and then cropped to 350×350-pixel squares to use as input data for stochastic reconstructions. The general scheme of the image processing and 3D input geometries preparation is shown in Fig. 1.

For stochastic reconstructions, we utilized a correlation function (CF) method based on a modified Yeong-Torquato technique [27]. For faster convergence and better accuracy, we also implemented hierarchical simulated annealing [39]. At first, the original 2D image is used to compute a set of two types of correlations functions: (1) the two-point probability function S_2 describing the probability that two points separated by a vector displacement $\mathbf{r}(x_1, x_2)$ between x_1 and x_2 lie in the same phase and (2) the lineal function L_2 describing the probability that the whole segment $\mathbf{r}$ lies within the given phase. Note that while S_2 is computed for the pore phase only, the lineal correlation function is computed separately for both pore and solid phases (black and gray on Fig. 1). There is no point in computing S_2 for both binary phases, as each one of them can be calculated from the other [40]. We calculate S_2 and L_2 in two orthogonal and two diagonal directions. Details of directional CF computation have been previously described elsewhere, and thus only a brief description is provided here; for more information please refer to Gerke *et al.* [41] and Karsanina *et al.* [30]. As we reconstruct the 3D structure, the third dimension is not known from the 2D input image and to estimate it we simply average CFs from two known dimensions. While not necessarily an accurate method in the case of reconstructing real anisotropic porous media, here we desirably create a different third dimension that should make more distinct off-diagonal terms of the permeability tensor.

For any set of correlation functions considered in the 3D reconstruction technique, matching correlation functions of a given realization with an original reference 2D image is based on voxel permutations. If a set of two-point correlation functions used in reconstruction is provided in the form of $f_2^\alpha(\mathbf{r})$, where α is a type of CF and $\mathbf{r}$ is a segment of varying length, then the difference between two realizations of the structure can be expressed as the sum of squared differences between sets of correlation functions [27,33]:

$$E = \sum_\alpha w_\alpha \sum_\mathbf{r} \left[f_2^\alpha(\mathbf{r}) - \hat{f}_2^\alpha(\mathbf{r}) \right]^2, \tag{1}$$
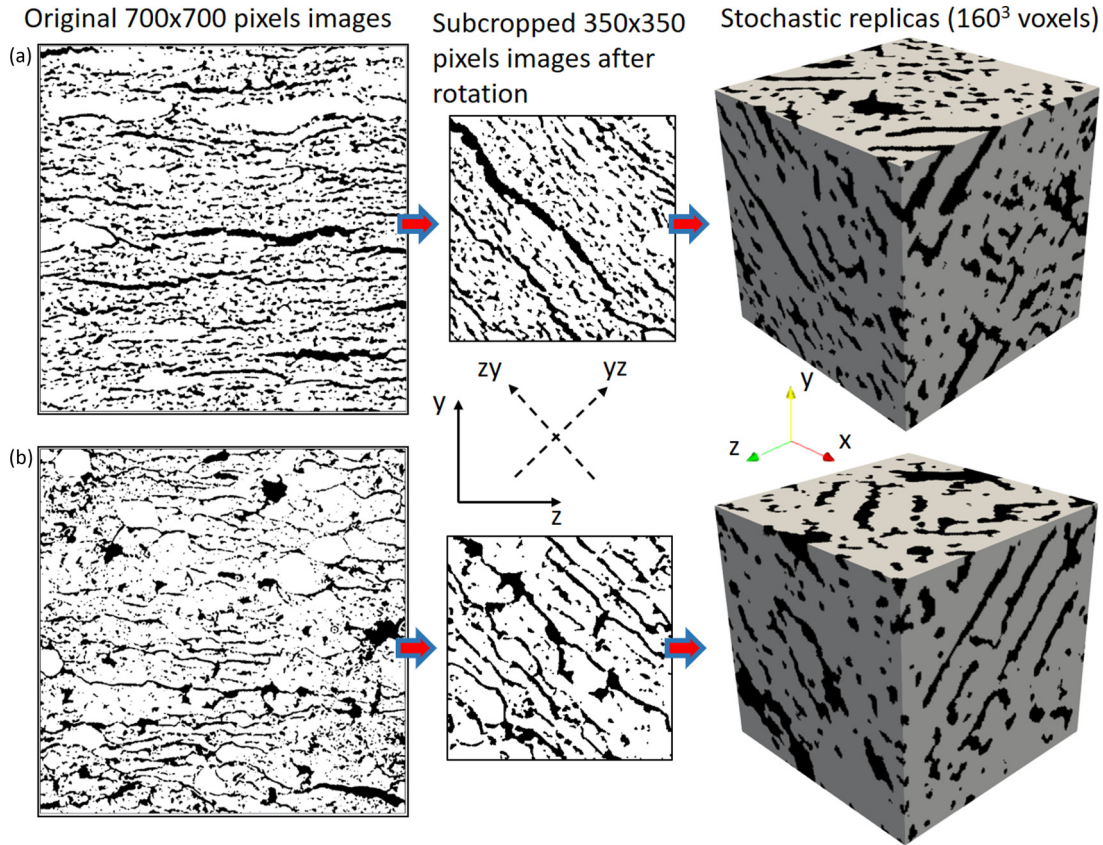
FIG. 1. General scheme of the image processing, 3D stochastic reconstructions, and preparation of the pore geometries for pore-scale simulations (pores are shown in black).

where $f_2^\alpha(\mathbf{r})$ and $\hat{f}_2^\alpha \mathbf{r}$ are the values of the CF sets for two realizations (where the former represents a reference 2D image while the latter represents the structure under reconstruction) and w_α is a weight factor used to improve convergence. In Eq. (1), E represents the "energy" of the system, which is minimized by the simulated annealing algorithm [42]. We start from a random structure and change voxel positions while checking the systems energy according to Eq. (1) and sequentially jump from coarser to finer scales [39]. The Metropolis algorithm is used [43] for the simulated annealing algorithm, which describes the probability p of accepting (or rejecting) every single random permutation of pixels between pore and solid phases in the following way:

$$p(E_{\text{old}} \rightarrow E_{\text{new}}) = \begin{cases} 1, & \Delta E < 0 \\ \exp(-\Delta E/T), & \Delta E \geqslant 0 \end{cases}, \quad (2)$$

where T is the so-called temperature of the system and

$$\Delta E = E_{\text{new}} - E_{\text{old}}. \quad (3)$$

The initial temperature T is chosen so that the probability p for $\Delta E \geqslant 0$ equals 0.5 [27]. We utilized the following cooling schedule based on the geometrical progression of the form:

$$T(k) = T(k-1)\lambda, \quad (4)$$

where k is time step and λ is a parameter smaller than but close to unity. We used the annealing schedule parameter $\lambda = 0.999999$ for all reconstructions.

To improve the speed of convergence, we adopted a relatively simple permutation approach following Čapek *et al.* [44] and Veselý *et al.* [45]: (1) choosing a random location within a phase of interest and (2) choosing two random directions in which two pairs of pixels with a minimum distance in-between are selected such that they satisfy the conditions of lying in opposite phases and at the interface. The size of all 3D reconstructions was 160^3 voxels, which is a good trade-off between the volume of the reconstruction and computational resources required later for flow simulations. We chose a cut-off length of $\mathbf{r} = 80$ for all CFs computations and stochastic reconstructions, which actually makes sense as this value is half of the reconstruction size. Periodic boundary conditions were applied for CFs evaluation during reconstruction procedure, which is critical to be able to apply desired flow modeling boundary conditions later. The reconstruction procedure was terminated after 10^6 consecutive unsuccessful permutations. Weight factors w_α in Eq. (1) were chosen according to the methodology described in Gerke and Karsanina [33].

After stochastic replicas were obtained as described above, we meshed the pore space only (as later we simulate single phase creeping flow within the pores). To mesh 3D pore geometries, we utilized a free Matlab toolbox iso2mesh [46]. While creating unstructured meshes, we varied meshing parameters, mainly the size of the maximum element (MES), to find a good trade-off between the coarseness of the mesh (relevant to CPU and RAM resources usage) and the accuracy
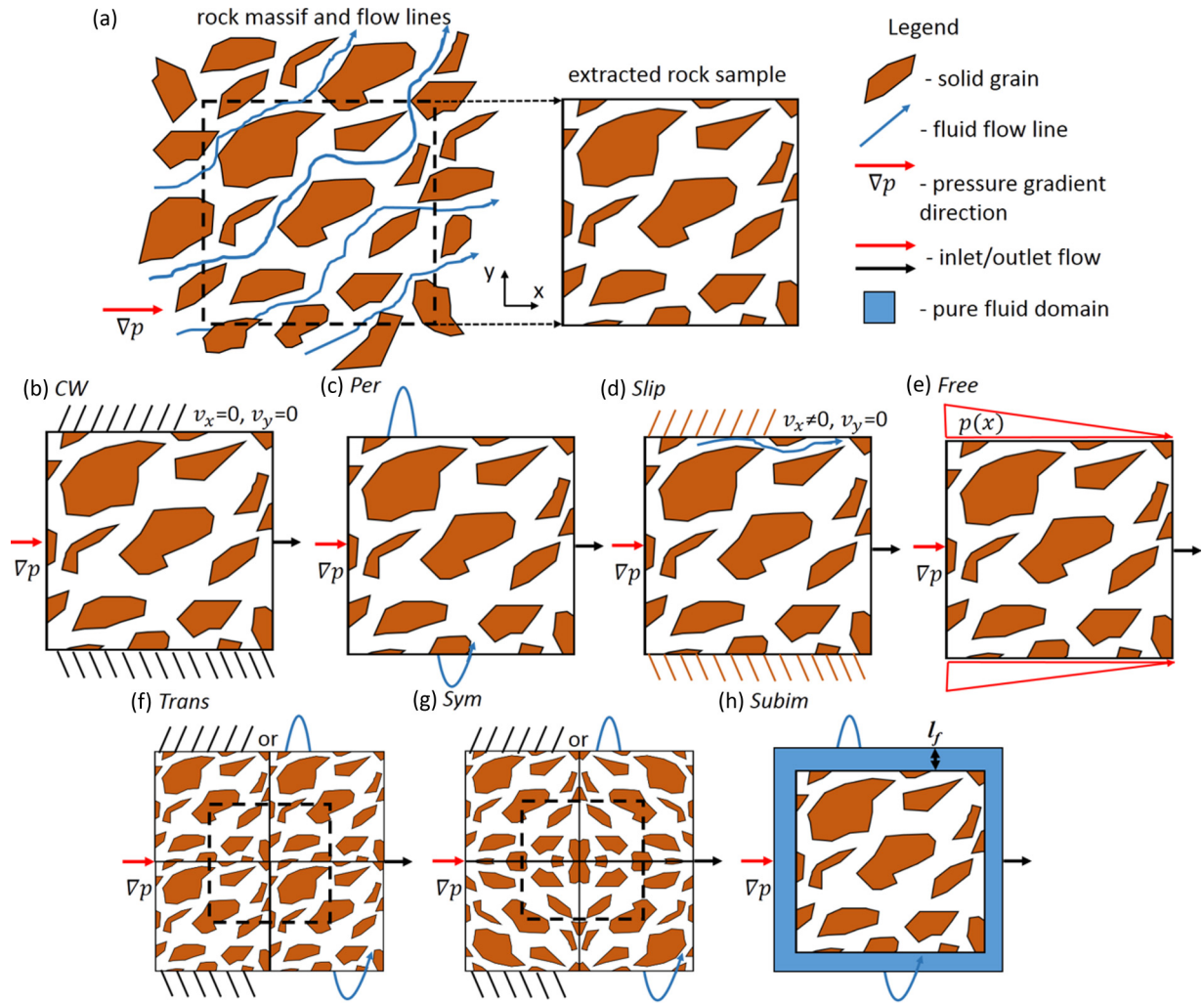
FIG. 2. Schematic diagrams of all boundary conditions explored shown in 2D for clarity: (a) the flow in real subsurface system containing the modeling domain, (b) CW BC, (c) Per BC, (d) Slip BC, (e) Free BC, (f) Trans BC, (g) Sym BC, and (h) Subim BC (a more-detailed description of each boundary condition is presented in the text).

of the solution (see the results of the mesh sensitivity study below).

B. Boundary conditions

In this subsection, we discuss all the BCs on the external walls of the modeling domain carried out in this study. For simplicity and in line with previously described 3D pore geometry reconstruction procedure, we work with cubical modeling domains which have six faces. Potentially, all BCs discussed below can be extended to noncubical modeling domains. The general scheme of all boundary conditions explored here is shown in Fig. 2, and all the major details are explained in the respective subsections below.

1. Closed walls

The first classic boundary condition, closed walls (CW), is probably the most commonly used for flow simulations [Fig. 2(b)]. It is a pressure imposed type of BC where one face serves as an inlet and the face opposing it serves as the outlet. A pressure gradient is imposed between inlet and outlet to

induce the flow. All four other faces of the cube parallel to the pressure gradient are treated as closed walls, thus simulating the permeameter laboratory measurement technique. This BC type is very easy to implement in most numerical methods, as the external walls have the same no-slip boundary condition as a pore-solid boundary in the rest of the modeling domain. However, this results in suppressed transversal flow within the sample.

2. Periodic

Periodic (Per) is another type of classical boundary condition where each face connects to the opposite face [Fig. 2(c)]. Simply put, the flow leaving the domain from one side re-enters from the other one. This is the most critical BC for our study and we created 3D stochastic reconstructions with periodic pore geometries to fully exploit all the possibilities from this boundary condition type. Transversal flow is, thus, allowed within the sample in a manner similar to being within a porous media massif [Fig. 2(a)]. Notably, this BC type was not studied in the work of Guibert *et al.* [18].
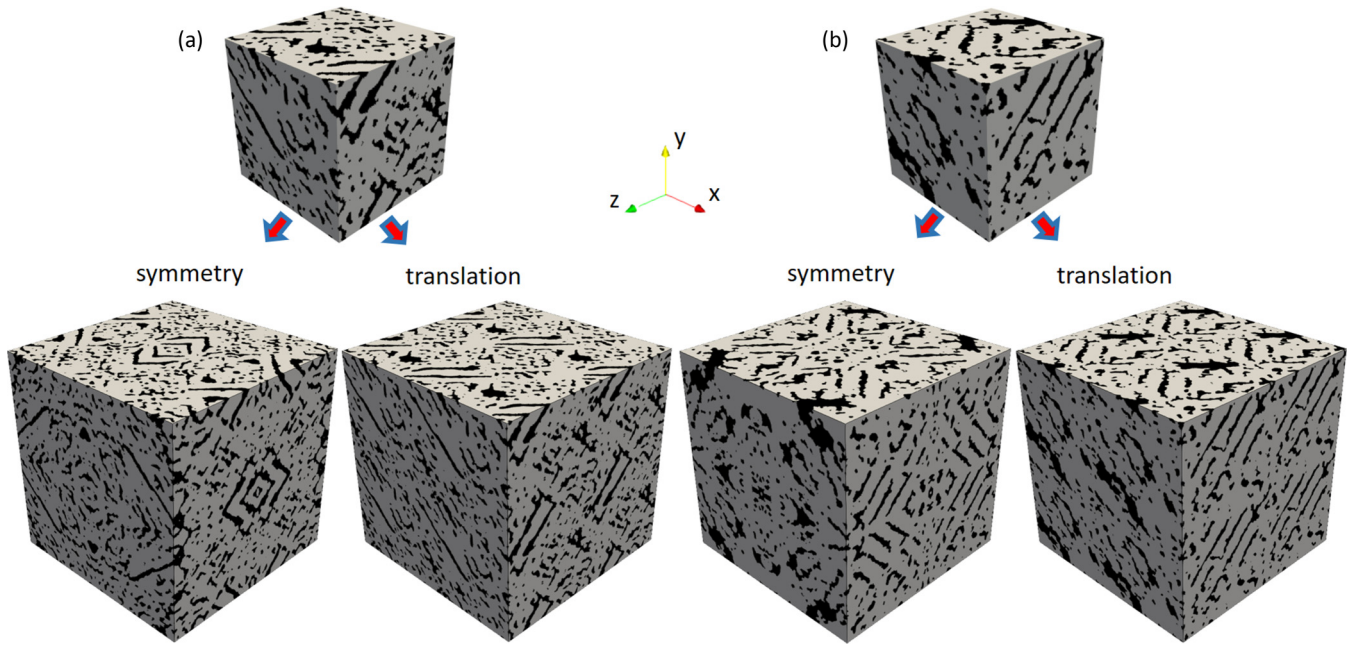
FIG. 3. Preparation of larger 3D images from original stochastic replicas by translation and symmetry for (a) shale and (b) soil samples (pores are in black).

3. Symmetry or slip on the walls

Symmetry or slip on the walls (Slip) represents an intermediate step between closed walls and periodic BCs [Fig. 2(d)]. The velocities tangential to the walls are allowed to develop as if there were no walls at all (slip flow), yet all velocities normal to the walls are zeros. This BC also suppresses transversal flow within the sample but partially circumvents the issue of no-flow boundary along all four faces of the modeling domain in terms of diagonal permeability tensor terms by allowing nonzero velocities along the boundaries. Note that this BC is also refered to as *free-slip BC* [47] and is not related to slip on the pore-solid boundaries, e.g., during rarefied gas flow.

4. Free or linear pressure

Free or linear pressure (Free) comes from Darcy-scale upscaling procedures [48] and tries to emulate the situation in Fig. 2(a) where fluid around the sample can enter and leave the sample depending on the local pressure conditions, thus allowing for transverse flow. In addition to the pressure imposed on inlet and outlet faces, all the other four faces parallel to the main pressure gradient have imposed pressures varying linearly along their length from inlet to outlet [Fig. 2(e)].

5. Translated and symmetrical configurations

As our 3D pore geometries are periodic, we can check the classical closure problem solution by geometrical translation and symmetry [49]. The idea of the translated and symmetrical configurations (Trans and Sym) boundary conditions is to allow transverse flow by connecting pores to the mirror image (symmetry) for nonperiodic pore structures. Simple translation may result in nonpercolating images (see Fig. 1 in Guibert *et al.* [18]) but applicable to our periodic images. Thus, we explore both options for completeness. The resulting 3D images are 8 times more voluminous and are shown

in Fig. 3. The flow is simulated using regular closed walls and periodic boundary conditions. We estimate permeability tensor in the whole image and in the center 160^3 voxels cube, as was previously done by Guibert *et al.* (2016).

6. Subvolume immersion

Subvolume immersion (Subim) is another way to promote the transversal flow in nonperiodic geometry configurations, which requires the immersion of the sample into a larger volume [Fig. 2(g)]. The novel approach of Guibert *et al.* [18] was to encapsulate the nonperiodic sample into some porous media (Darcian scale) and to iteratively adjust its permeability tensor so that it would equal the computed tensor for the whole domain. This very interesting idea is actually quite simple: to immerse the sample in the same periodic (thanks to Darcian continuum-scale representation, the nonperiodicity of the pore geometry is not an issue any more) porous media, thus creating realistic boundary conditions as in Fig. 2(a), although we do not implement the same approach exactly, as this condition is already fulfilled within our stochastic reconstructions. However, to further elucidate some important aspects of the immersion technique we considered its modification: immersion of the sample into the fluid which can freely flow in and out of the sample. The width of the fluid layer l_f is the parameter of this type of boundary condition (and excluded from the analysis during tensor evaluation). Pressure gradient is applied through inlet and outlet faces, while all the other four faces are treated with periodic BCs.

C. Numerical methods

In order to compute permeability tensor, we solve Stokes's equation within 3D pore geometries to simulate flow with low

Reynolds number, referred to as creeping flow:

$$\begin{cases} \mu \Delta \vec{v} - \nabla p = 0 \\ \nabla \cdot \vec{v} = 0 \end{cases}, \qquad (5)$$

where $\vec{v}$ is velocity field, μ is fluid viscosity, and p is pressure field. No-slip boundary condition is maintained across all pore-solid interfaces. If pressure boundary conditions are applied, one can solve this problem numerically to obtain velocity field, which we do using two different methods: (1) finite-difference Stokes solver (FDMSS) [16] and (2) FEM-based commercial software Comsol Multiphysics, v5.3. The reason we utilize two different methods lies with the wide variety of boundary conditions and computational resources needed to obtain a solution.

The FDMSS software is computationally efficient, operates on voxel-based images such as shown in Figs. 1 and 3, and has CW and Per BCs already implemented. Other BCs are not simple to implement within a staggered grid scheme, except for Subim, which simply required an addition of fluid voxels around the 3D pore geometry (which was done separately by creating a larger 3D input geometry). The Trans and Sym BCs were also naturally easy to implement, as those are the special case of Per BC after a new geometry configuration is created. For more details on the FDMSS methodology, see Gerke *et al.* [16].

Flow modeling with Comsol Multiphysics requires meshing and more abundant computing resources, especially RAM. But it provides a number of very powerful choices to implement boundary conditions, namely Slip BC using the "Symmetry" condition on four faces of the cubic domain parallel to the pressure gradient, and Free BC using "Inlet" and "Outlet" conditions with unchecked suppressed back-flow and a linear pressure gradient along each of the four faces. The choice of fluid discretization affects the quality of the solution, so we explored a number different options, namely P1+P1, P2+P1, and P2+P2 for velocity and pressure (which guarantee the global conservation) options, respectively. We chose a parallel sparse direct solver (PARDISO), which proved to be a good compromise among stability, RAM, and CPU time requirements.

All input parameters for both FDMSS and Comsol simulations (e.g., fluid viscosity and pressure gradient) were adjusted in such a way that all resulting flow velocities would be in pixels per second and permeability in pixels squared (i.e., the unit size of the lattice of the stochastically reconstructed images). Using pixels as dimensionless units is convenient to combine the results, as no comparison of computed permeabilities against measured real data was performed.

D. Tensor evaluation

The permeability tensor is computed according to Darcy′s law:

$$\mathbf{K} = -\frac{\mu \phi \langle \vec{v} \rangle}{\nabla p}, \qquad (6)$$

where $\langle \vec{v} \rangle$ is the average flow velocity vector coming as the solution of Stokes's flow problem, ϕ is the porosity of the 3D image, and ∇p is pressure gradient. If ∇p is imposed in three orthogonal directions and pressure and velocity fields

p and $\vec{v}$ are assessed numerically by solving Eq. (5), then the full-permeability second-rank tensor can be evaluated. For our cubic modeling domains, we apply a pressure gradient in three major orthogonal directions, x, y, and z, and solve the following system of linear equations to obtain tensor $\mathbf{K}$:

$$\begin{pmatrix} v_x^x & v_x^y & v_x^z \\ v_y^x & v_y^y & v_y^z \\ v_z^x & v_z^y & v_z^z \end{pmatrix} = -\frac{1}{\mu\phi} \begin{pmatrix} K_{xx} & K_{xy} & K_{xz} \\ K_{yx} & K_{yy} & K_{yz} \\ K_{zx} & K_{zy} & K_{zz} \end{pmatrix}$$

$$\times \begin{pmatrix} \nabla p_x^x & \nabla p_x^y & \nabla p_x^z \\ \nabla p_y^x & \nabla p_y^y & \nabla p_y^z \\ \nabla p_z^x & \nabla p_z^y & \nabla p_z^z \end{pmatrix}, \qquad (7)$$

where superscripts for flow velocity and pressure fields refer to the orientation of the imposed pressure gradients and subscripts represent the direction of the solution, both along the same major x, y, and z axes. The transverse (subscript $\neq$ superscript) pressure gradients on the right-hand side of Eq. (7) are computed based on results of the numerical solution of the Stokes equation [Eq. (5)] by averaging pressure values, p, between the opposed faces of the modeling domain. To elucidate the importance of the diagonal transverse pressure gradients we also compute permeability tensor $\mathbf{K}_0$, which is also frequently used in the literature:

$$\begin{pmatrix} v_x^x & v_x^y & v_x^z \\ v_y^x & v_y^y & v_y^z \\ v_z^x & v_z^y & v_z^z \end{pmatrix} = -\frac{1}{\mu\phi} \mathbf{K}_0 \begin{pmatrix} \nabla p_x^x & 0 & 0 \\ 0 & \nabla p_y^y & 0 \\ 0 & 0 & \nabla p_z^z \end{pmatrix}. \qquad (8)$$

While it is well established that the permeability tensor is symmetrical [50], the numerical solution of Eqs. (7) and (8) usually results in nonequal corresponding off-diagonal terms [14,15,18,51]. Therefore, it is a common practice to symmetrize it, for instance, by:

$$\mathbf{K}_{\text{sym}} = \tfrac{1}{2}(\mathbf{K} + \mathbf{K}^T). \qquad (9)$$

The second approach (usually referenced to as the Durlofsky method according to the corresponding paper) is to enforce symmetry by adding additional constrains while solving Eq. (7) or Eq. (8) [52,53]:

$$\begin{cases} \text{Eq. (7) or Eq. (8)} \\ K_{xy} = K_{yx} \\ K_{zx} = K_{xz} \\ K_{zy} = K_{yz} \end{cases} . \qquad (10)$$

We shall routinely report the results of tensor permeabilities $\mathbf{K}$ and $\mathbf{K}_0$ calculations for both soil and shale samples according to all boundary conditions described in Sec. II B. The values of $\mathbf{K}_{\text{sym}}$ [Eq. (9)] and that according to the Durlofsy method [Eq. (10)] were also computed but will be reported only in relevant special cases to highlight their potential usefulness.

III. RESULTS AND DISCUSSION

A. Major properties of 3D pore geometries

The 3D stochastic reconstructions rendering of the pore space is shown in Fig. 4 together with two-point probability and lineal correlation functions computed in different directions for each sample of pore phase. As expected from the
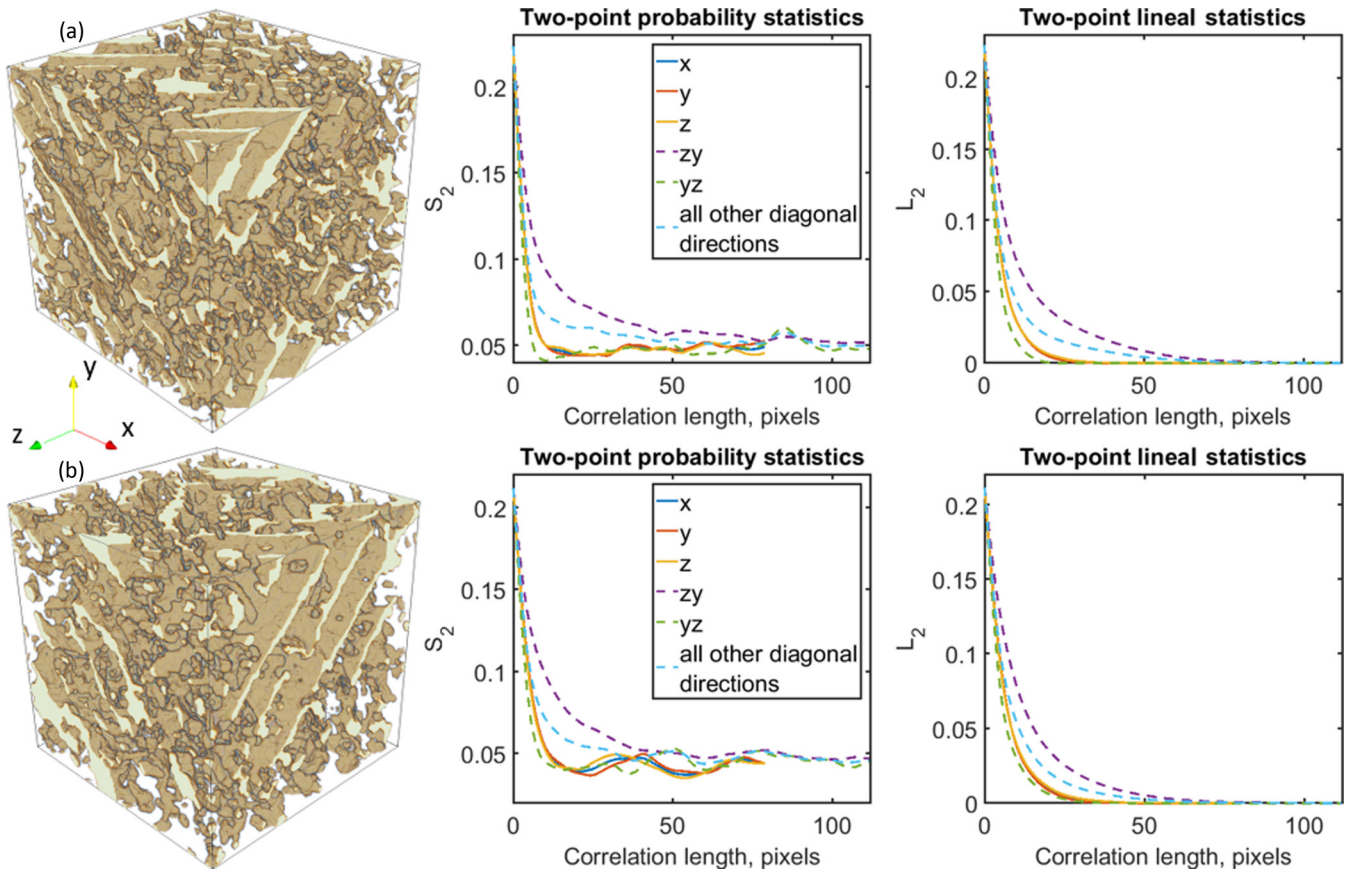
FIG. 4. The rendering of the pore geometry in 3D and directional two-point probability and lineal correlation functions for 3D stochastic replicas of (a) shale and (b) soil. The y and z directions are similar to original images shown in Fig. 1, while the x direction is the one deduced as their average (according to correlation function statistics as shown on the right side).

input 2D geometries (Fig. 1), the most connected is the diagonal zy direction, while yz is the least-connected one. All other diagonal directions are between those two as by the design of the reconstruction procedure. Note that in Fig. 4 the diagonal correlations are computed to longer lengths; this is due to the fact that the diagonal of the voxel is $\sqrt{2}$ larger than its side. The major orthogonal directions are almost the same in terms of both correlation functions with the y direction being only slightly more connected than z, with x (the average) lying in between. All S_2 reach values close to ϕ^2 with increasing correlation length and all L_2 decay to 0. This indicates that 3D pore geometry can be considered as representative elementary volume (REV) according to correlation functions statistics [44,54]; note that the correlation length shown is half of the actual 3D cubical image with the volume of 160^3 voxels. It is important to highlight that this REV is purely morphological and does not guarantee REV for permeability (which we shall study later on after establishing correct BCs). The aim of the stochastic reconstruction was to create a complex and highly anisotropic structure with possible large off-diagonal terms of permeability tensor. The visualization of the pore geometry in Fig. 4, as well as correlation functions statistics, both suggest that the 3D images created satisfy these requirements and could be loosely described as porous samples with transversely oriented cracks highly connected by smaller pores spanning in all directions. The connectivity was also checked

by computing directional cluster correlation function, which was very close to two-point probability S_2 (and, thus, not shown here), as pores mainly formed one large cluster.

B. Mesh sensitivity and validation of consistency between FDMSS and Comsol solutions

The unstructured meshes for both samples, which were used for simulations with Comsol, are shown in Fig. 5. Note that while FDMSS automatically addresses the problem of unconnected porosity, for meshing purposes all such pore voxels were removed with the help of Hoshen-Kopelman clustering. The meshing parameter of maximum element size was chosen based on mesh sensitivity study, which was

TABLE I. The results of the mesh sensitivity study: The influence of the mesh coarseness on the solution obtained.

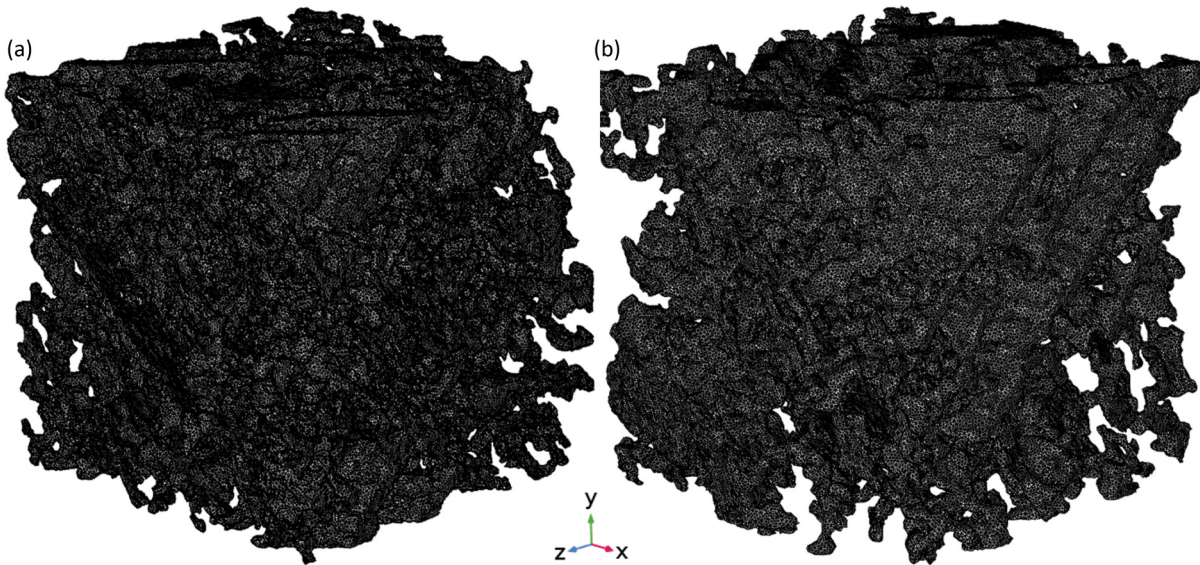| MES (voxels)	Total number of elements in the mesh	Permeability error($= \frac{\text{Value}}{\text{Reference}} - 1$)
10	450 329	-3.22×10^{-1}
3	474 684	-3.20×10^{-1}
1.5	732 465	-2.04×10^{-1}
1	1 453 080	-3.79×10^{-2}
0.75	4 242 978	0

FIG. 5. The meshes used to perform simulations with Comsol for (a) shale and (b) soil samples.

carried out on five meshes of different coarseness. For each mesh, we simulated flow in the x direction using CW boundary conditions. The results of the simulations for the soil sample are shown in Table I for P2+P1 fluid discretization. While P1+P1 required significantly fewer RAM and CPU resources, computed velocities or permeabilities were significantly lower than with other discretizations. As P2+P1 (default recommended Comsol parameter for Stokes flow simulations) had only 1.5–3% error compared to P2+P2 for soil and shale samples, we decided to utilize P2+P1 for all computations. Based on the results in Table I we concluded that the meshes with a maximum element size of 1 voxel are optimal for simulations, as they have shown only −3.8% error compared to MES = 0.75. The change of MES from 1 to 0.75 resulted in an increase in the number of mesh elements of 2.9 and such <5% increase in accuracy is not compensated for by the significant rise of computational resources demands.

Now we need to verify whether FDMSS and Comsol solutions are consistent, i.e., they provide similar permeability tensors for the same pore geometry and boundary conditions. To do so, in addition to complex Free and Slip BCs, we also simulated simple WC boundary conditions for both samples with Comsol. In Table II we now compare **K** evaluated according to Eq. (7) with transverse pressure gradients

between two computational approaches. It is clear that the congruence between FDMSS and Comsol tensors is not perfect; in particular, we observe some large discrepancies between major orthogonal directions—the xx term is lower for FDMSS soil sample numerical solution, while for shale sample the yy and zz terms are lower for Comsol. We see two obvious reasons why solutions with two different methodologies are disparate here: (1) The FDM and FEM methods have different sensitivity to the original voxelized 3D image discretization (i.e., its quality in terms of resolution-to-characteristic pore size ratio) and (2) some pore connectivity losses during meshing. The loss of connectivity is the second reason, but it was probably unclear because of due to some pore connectivity losses during meshing. The first problem is complex; however, sensitivity of different pore-scale modeling approaches to the 3D image quality is a topic of current active research [14,16,55,56]. Due to the high anisotropy of the 3D pore geometries under study, the accuracy of the FDM voxel-based and FEM mesh-based solution may differ locally within the sample and such differences result in the observed discrepancies. The second problem can be seen on some Comsol-based pressure field visualizations [e.g., Fig. 7(c)], but we could anticipate negligible effect from such small disconnected pore clusters, as they disappear with MES = 0.75 and the accuracy of the solution with MES = 1 is

TABLE II. Comparison of full permeability tensors **K** with transversal pressure gradients accounted for as obtained for closed walls boundary conditions using FDMSS and Comsol modeling frameworks.

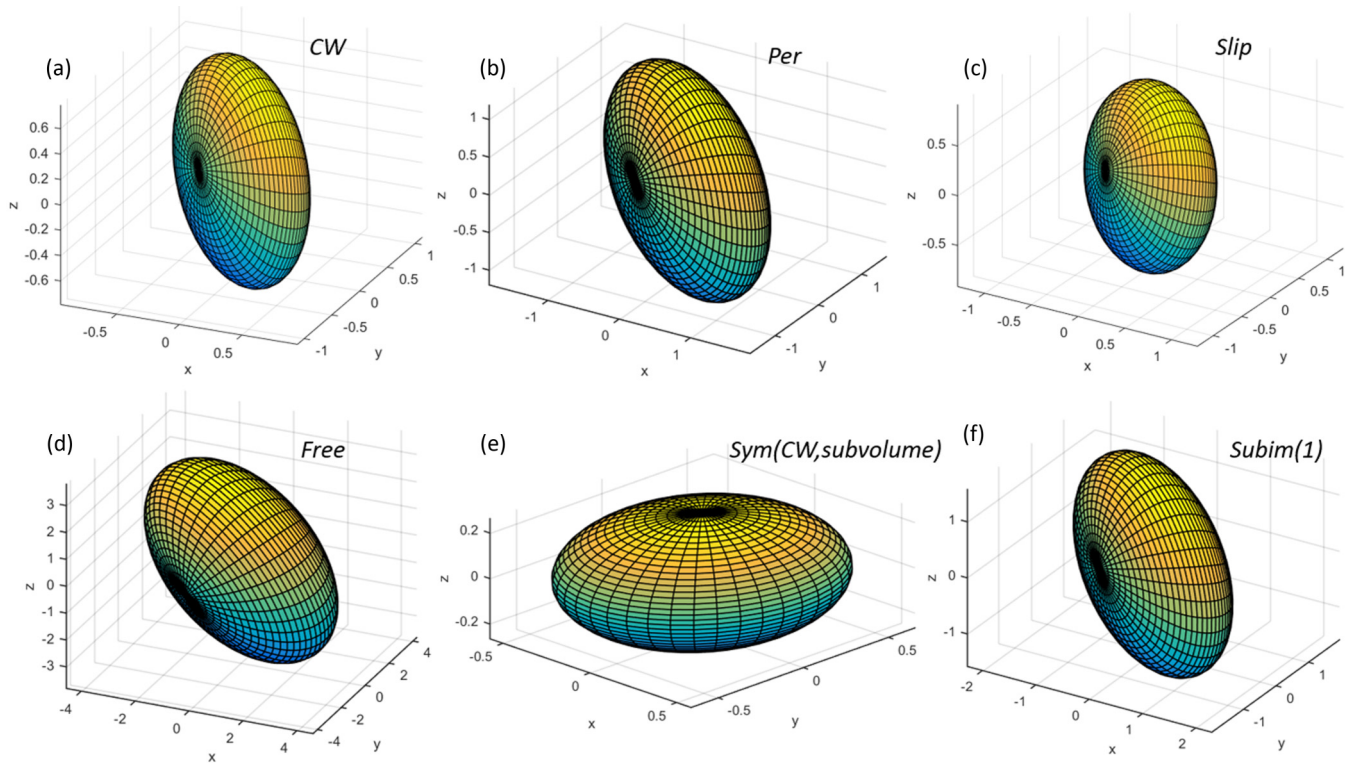| Sample	FDMSS $\mathbf{K}(ij)$ (voxels^2)			Comsol $\mathbf{K}(ij)$ (voxels^2)		
Shale	0.010529	−0.00504	−0.00188	0.010722	−0.00492	−0.00102
	−0.00827	0.015045	−0.00104	−0.0061	0.010819	−0.00078
	−0.00083	−0.0006	0.014869	−0.00052	−0.00055	0.012007
Soil	0.019636	−0.01322	0.004433	0.024534	−0.019	0.008274
	−0.01391	0.025435	−0.00015	−0.01372	0.024534	−0.0016
	−0.00046	0.0018	0.019562	0.001664	0.000277	0.019719

FIG. 6. Visualization of tensorial permeabilities for the shale sample using 3D ellipsoids (color shading of ellipsoids does not represent any values and is solely for visual purposes): (a) CW, (b) Per, (c) Slip, (d) Free, (e) Sym (CW, subvolume), and (f) Subim (one pixel) boundary conditions. Note that coordinate system positioning and magnitude are not the same for each subplot due to visibility issues.
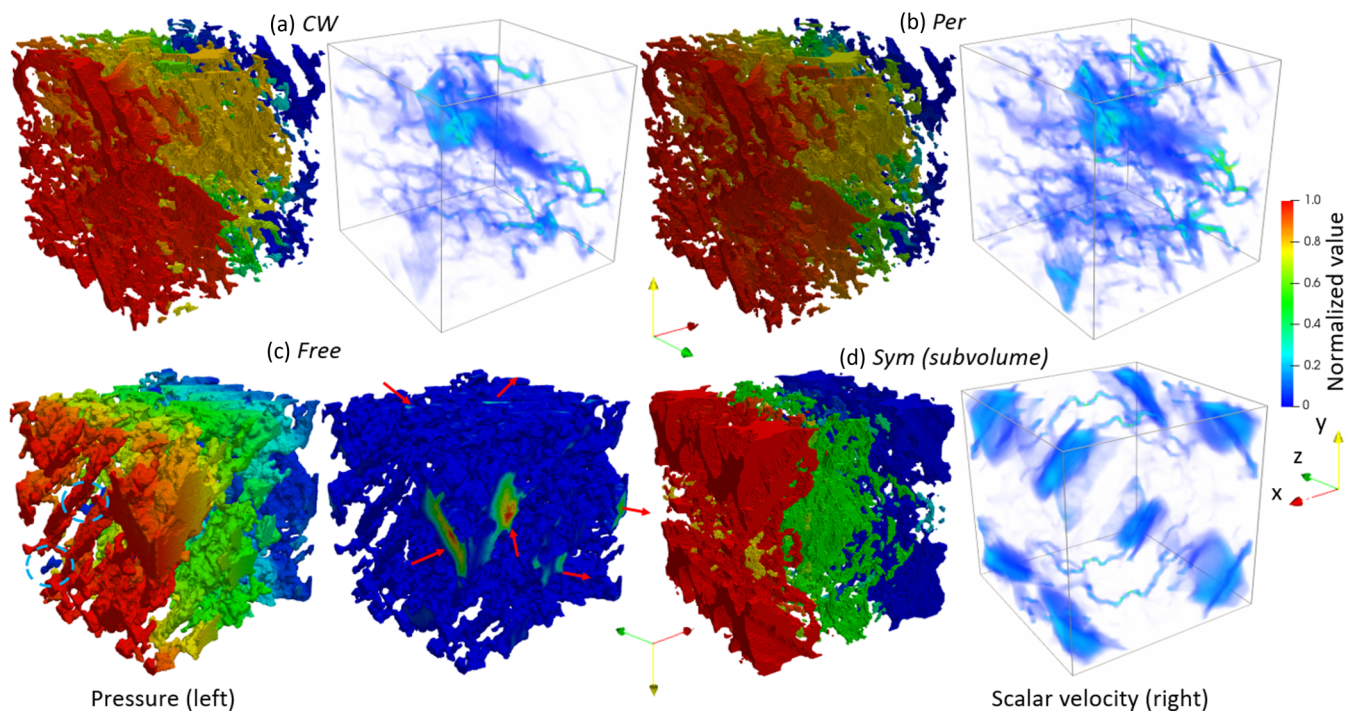

FIG. 7. Visualization of simulated pressure (left) and velocity (right) fields under different boundary conditions: (a) CW, (b) Per, (c) Free, (d) Sym (CW, subvolume).

only 3.8% different. Nonetheless, as qualitative deviations along orthogonal directions are moderate and we actually observe general correspondence between FDMSS and Comsol solution in terms of sign and magnitude for off-diagonal terms, the accuracy of the solutions with these two methods is more than satisfactory to address the main aim of our study and analyze the influence of boundary conditions on permeability tensor.

C. Influence of boundary conditions on permeability tensor: Results

The main results of this paper demonstrating tensorial permeabilities [as computed using Eq. (7) and Eq. (8)] for shale and soil samples depending on all the investigated boundary conditions are presented in Table III and Table IV. For better readability and ease of comparison, all terms have been normalized by a maximum value in the CW boundary condition for **K** tensor.

From the presented results it is clearly evident that except for the Sym boundary conditions all obtained tensors are nonsymmetrical. While it is well established that Stokes's flow should result in periodic boundary conditions [50,57], unless Eq. (9) is used, pore-scale computations in the literature usually report significant nonsymmetry (e.g., Refs. [14,15,18,51]. Our experimentation with Eq. (10), which produces overdetermined system of equations, also generated nonsymmetrical tensors and, thus, they are not reported here due to the lack of usefulness from this approach.

The influence of transverse boundary conditions is as expected: For all CW-based, except Sym, conditions K_0 usually has somewhat lower values as compared to **K**. For Per-based conditions the difference is tantamount to simulation errors due to zero transverse gradients. The same is observed for Sym subvolume cases where these gradients are also practically zero. The Free boundary condition has zero transversals by definition (linear pressure drop on all faces parallel to applied pressure gradient). From the computational point of view, obtaining K_0 and **K** presents very little difference compared to the expensive Stokes flow solution. In this light, computing **K** at all times is a simple strategy to prevent any misinterpretation. Thus, we shall consider only Eq. (7) (full tensor with transversal pressure gradients) results from now on.

For visualization purposes, it is convenient to compute the eigenvector of the permeability tensor. This is very useful in terms of permeability orientation, which in this regard is more visually informative than the raw tensorial data in Tables III and IV. Figure 6 depicts permeability tensors in such a way that both orientation and magnitude are evident.

From Fig. 6 visualizations, we observe that boundary conditions not only significantly affect magnitude but also the orientation of the flow. Boundary conditions that are not shown, namely Trans and multiple subversions of Sym and Subim, are omitted as they are generally similar to CW and Per (depending on the side faces flow conditions), e.g., Fig. 6(e) and Fig. 6(f), respectively. Notably, the Per and Subim boundary conditions show identical orientations. Both the orientation and magnitude of the permeability tensor are of utmost importance for upscaling, transport, and Darcian-

scale modeling (e.g., Refs. [53,58–60]). Understanding of the observed differences requires interpretation of the pressure and velocity fields for each boundary condition, which is presented in the following subsection.

D. Influence of boundary conditions on permeability tensor: Interpretation

We carefully analyzed the pressure and velocity fields for the modelled boundary conditions; some of the most interesting cases are visualized in Fig. 7. We start with the comparison of the CW and Per cases in Figs. 7(a) and 7(b). While pressure fields (images on the left sides) look quite similar, they are actually very different in terms of transversal pressure gradients: Due to friction along the walls, CW produced significant transversal pressure differences, while Per BCs produced none. Flow fields for these two cases look very different due to the absence and presence of transversal flow. Periodic flow resulted in higher velocities and their orientation along major anisotropy (Fig. 4), thus producing tensors with different orientations and higher magnitudes (Fig. 6). Such behavior is expected and was previously observed when computing permeabilities for stochastic reconstructions [33]. The Slip boundary condition produced pressure and velocity fields somewhat similar to CW (thus not shown here) with only one obvious difference: Velocities along the closed walls were higher, which slightly affected orientation and magnitude of the permeability tensor compared to CW case. The Free boundary condition clearly stands out from all other BC types and produces very specific flow velocity field [e.g., Fig. 7(c)]. While the pressure field generally looks similar to that of other types, its linear pressure drop with free boundaries produces inflow into the domain closer to high-pressurized walls and outflow later [see the red arrow in Fig. 7(c), which highlights such inflow and outflow areas]. Each domain wall along the applied pressure gradient exhibits similar behavior in terms of such inflow-outflow areas creating convection-like zones within the domain. This severely affects both magnitude (roughly 5 times higher for Free compared to CW) and direction of the permeability tensor [Fig. 6(d)]. All Trans BCs, including both with CW and Per walls, produced pressure and flow velocity fields similar to pure CW and Per cases, respectively. This is simply due to the fact that we have increased the volume of the modeling domain by 8 times by replicating the same 160^3 voxels cubes (i.e., tiling as shown in Fig. 3). The situation with subdomains is the same as for full domains as subvolumes are the same original 160^3 voxels images translated by half of their width. We note that the Trans results are interesting only from the viewpoint of the modeling domain size (as will be discussed shortly), but its relevance for computing tensorial flow properties is limited, due to the fact that for real 3D images translation does not work due to the absence of geometrical periodicity [18]. The Sym case is very different from Trans and all other BCs. While original 160^3-voxel volumes may behave similarly in terms of pressure and flow velocity fields, the total picture for the whole 320^3-voxel symmetry images or their subvolumes [Fig. 7(d)] differs, as transversal flows within each subdomain negate each other. This results in zero off-diagonal terms in the permeability tensor [Fig. 7(e)], which also makes Per flow

TABLE III. Tensorial permeabilities for shale sample (normalized by 0.015 voxels^2).

BC	Normalized $\mathbf{K}_0(ij)$, –			Normalized $\mathbf{K}(ij)$, –		
CW (FDMSS)	0.625842	−0.295635	−0.135928	0.699821	−0.33466	−0.12484
	−0.324703	0.950339	−0.081833	−0.54962	1	−0.06897
	−0.072938	0.068225	0.991104	−0.05533	−0.04005	0.988281
Per	1.05397	−0.59485	0.034402	1.044269	−0.58005	0.037978
	−0.690596	1.582546	−0.004304	−0.66464	1.573106	−0.01643
	−0.080391	−0.039526	1.329646	−0.08657	−0.04494	1.330111
Slip	0.687662	−0.27606	−0.08101	0.787254	−0.32677	−0.07508
	−0.21518	0.760297	−0.06491	−0.4231	0.810441	−0.05751
	−0.04668	0.058638	0.868719	−0.02742	−0.04216	0.869402
Free	2.541671	−0.991134	0.074258	2.526086	−0.82472	0.019246
	−0.945979	2.589404	−0.695846	−0.81475	2.558462	−0.78376
	0.15541	−0.63308	3.141695	−0.00615	−0.6794	3.186392
Trans (CW) full	0.638734	−0.250758	−0.034239	0.729199	−0.36995	−0.02588
	−0.341701	1.104178	−0.011671	−0.63868	1.210328	−0.03468
	−0.025137	0.022512	1.010688	−0.01508	−0.00592	1.010756
Trans (CW) subvolume	0.675044	−0.265368	−0.011888	0.75305	−0.40705	0.020285
	−0.31321	1.237633	−0.024563	−0.57071	1.345179	−0.04903
	0.00564	0.00683	1.023349	0.02249	−0.00261	1.024309
Trans (Per) full	0.902453	−0.563199	0.0211765	0.897933	−0.55749	0.022706
	−0.606876	1.476957	−0.009506	−0.59511	1.473173	−0.01562
	−0.025059	−0.02313	1.166177	−0.03005	−0.0234	1.166321
Trans (Per) subvolume	0.778853	−0.588079	0.020205	0.788545	−0.5981	0.030706
	−0.485918	1.409963	−0.013118	−0.50823	1.416461	−0.02679
	0.016321	−0.007410	1.0297101	0.030925	−0.01373	1.030057
Sym (CW) full	0.725804	4.8×10^{-8}	1.2×10^{-8}	0.725804	4.65×10^{-8}	1.18×10^{-8}
	-3.9×10^{-8}	0.975732	-1.1×10^{-8}	-3.4×10^{-8}	0.975732	-1.2×10^{-8}
	-2.7×10^{-8}	-1.9×10^{-8}	1.010865	-2.2×10^{-8}	-2.2×10^{-8}	1.010865
Sym (CW) subvolume	0.429754	1.6×10^{-7}	-1.9×10^{-8}	0.429755	1.32×10^{-7}	-1.6×10^{-8}
	-1.6×10^{-8}	3.048603	3.7×10^{-8}	-3.8×10^{-9}	3.048603	6.94×10^{-8}
	-8.9×10^{-9}	-3.4×10^{-7}	2.694853	1.17×10^{-8}	-3.3×10^{-7}	2.694853
Sym (Per) full	0.0.729244	3.7×10^{-8}	1.2×10^{-8}	0.729244	3.71×10^{-8}	1.24×10^{-8}
	-2.9×10^{-8}	1.026878	5.0×10^{-9}	-2.9×10^{-8}	1.026878	5.2×10^{-9}
	-4.2×10^{-8}	-1.8×10^{-8}	1.013677	-4.2×10^{-8}	-1.8×10^{-8}	1.013678
Sym (Per) subvolume	0.429826	8.2×10^{-8}	-4.1×10^{-8}	0.429826	7.32×10^{-8}	-4.7×10^{-8}
	1.8×10^{-8}	3.073092	1.1×10^{-7}	2.85×10^{-8}	3.073092	1.9×10^{-8}
	-4.4×10^{-8}	1.7×10^{-7}	2.678078	-4.5×10^{-8}	1.74×10^{-7}	2.678078
Subim ($l_f = 1$ voxel)	1.820209	−0.857433	0.037559	1.802971	−0.83716	0.043159
	−0.861077	2.02946	−0.146302	−0.81897	2.021031	−0.16442
	0.012022	−0.181073	1.94148	−0.00765	−0.19159	1.943308
Subim ($l_f = 5$ voxels)	3.284926	−1.203717	−0.044104	3.265777	−1.17478	−0.03622
	−1.192515	3.372159	−0.658691	−1.13029	3.367408	−0.68809
	−0.036891	−0.654005	3.804991	−0.08352	−0.68338	3.811216
Subim ($l_f = 30$ voxels)	6.965928	−1.737805	−0.624981	6.952155	−1.70134	−0.59566
	−1.661312	7.11751	−1.3273335	−1.57533	7.122699	−1.38639
	−0.414468	−1.1955163	7.754522	−0.48461	−1.26633	7.763253

conditions on the walls the same as CW due to mirroring on these walls. Finally, Subim produces the same normalized pressure and velocity fields, but they are different in magnitude due to the influence of the fluid layer outside of the porous media domain. This case produces the same orientation of the tensor but much larger permeability values.

While the highlights of Fig. 7 provide some general visual information about the flow field, such visualizations are not enough to depict all the local separate components that are important to produce the resultant tensor [Eq. (7)]. To further visually explain the difference between different investigated boundary condition cases, in Fig. 8 we present a general scheme (2D for simplicity and in the same manner as was

TABLE IV. Tensorial permeabilities for soil sample (normalized by 0.0254 voxels^2).

BC	Normalized $\mathbf{K}_0(ij)$, –			Normalized $\mathbf{K}(ij)$, –		
CW (FDMSS)	0.547783	−0.079084	0.020259	0.772017	−0.51963	0.174304
	−0.112857	0.690753	0.166672	−0.54685	1	−0.00583
	0.018278	0.078852	0.778622	−0.01819	0.070778	0.769121
Per	1.682165	−0.862225	0.041116	1.692362	−0.86587	0.051751
	−0.685779	1.309949	0.072154	−0.70173	1.310782	0.069725
	0.018862	0.099922	1.191890	0.01359	0.09105	1.19218
Slip	0.769833	−0.1765	0.055905	1.163081	−0.75374	0.335401
	−0.11376	0.724942	0.172323	−0.53981	1.043933	−0.06637
	0.007686	0.062311	0.839652	0.066886	0.009569	0.849702
Free	4.215826	−1.645263	−0.043003	4.255221	−1.53345	0.033788
	−1.641811	4.023835	−0.90001	−1.68128	3.977891	−0.75599
	−0.061798	−0.942343	3.745335	0.03758	−0.83675	3.733831
Trans (CW) full	0.725940	−0.218769	0.020731	0.91852	−0.59007	0.058104
	−0.238556	0.802090	0.073350	−0.57492	1.035091	0.052365
	0.019491	0.063729	0.904490	0.006135	0.067334	0.904998
Trans (CW) subvolume	0.745443	−0.2479446	0.026053	0.927912	−0.60521	0.012345
	−0.241912	0.829956	0.09077	−0.55928	1.050741	0.129866
	0.021595	0.059433	1.043203	−0.01451	0.106623	1.047785
Trans (Per) full	1.218578	−0.688238	0.008969	1.221944	−0.68754	0.008753
	−0.631726	1.160912	0.102033	−0.63752	1.160179	0.103104
	0.004945	0.113560	1.116849	0.003323	0.109703	1.116982
Trans (Per) subvolume	0.981353	−0.692438	−0.035034	0.985458	−0.68839	−0.03652
	−0.527622	1.058120	0.127789	−0.53442	1.054958	0.126735
	−0.008608	0.120974	1.049175	−0.01669	0.111401	1.048928
Sym (CW) full	0.640853	-1.6×10^{-8}	-7.9×10^{-9}	0.640853	-1.3×10^{-8}	-6.5×10^{-9}
	-8.6×10^{-9}	0.714769	-6.5×10^{-9}	-5.4×10^{-9}	0.714769	-4×10^{-10}
	3.2×10^{-8}	2.6×10^{-8}	0.801697	3.26×10^{-8}	3.67×10^{-8}	0.801698
Sym (CW) subvolume	0.577481	-5.6×10^{-8}	1.2×10^{-8}	0.577481	-1.2×10^{-8}	9.36×10^{-9}
	-1.9×10^{-8}	0.657982	-1.3×10^{-8}	-8.5×10^{-9}	0.657983	-1.8×10^{-10}
	1.9×10^{-8}	4.1×10^{-8}	0.264680	2.01×10^{-8}	3.73×10^{-8}	0.26468
Sym (Per) full	0.643011	4.1×10^{-8}	-2.2×10^{-8}	0.643011	4.11×10^{-8}	-2.2×10^{-8}
	-7.2×10^{-9}	0.716719	-2.7×10^{-8}	-6.9×10^{-9}	0.71672	-2.7×10^{-8}
	1.8×10^{-8}	3.3×10^{-8}	0.803523	1.83×10^{-8}	3.31×10^{-8}	0.803523
Sym (Per) subvolume	0.577520	-6.4×10^{-8}	-2.8×10^{-8}	0.57752	-4.5×10^{-8}	-2.6×10^{-8}
	-2.6×10^{-8}	0.657974	8.1×10^{-9}	-2.6×10^{-8}	0.657974	6.34×10^{-9}
	3.7×10^{-8}	3.4×10^{-8}	0.264646	3.67×10^{-8}	2.96×10^{-8}	0.264647
Subim ($l_f = 1$ voxel)	2.090728	−0.999958	0.094767	2.099355	−1.00028	0.102494
	−0.8969784	1.699184	−0.003424	−0.91299	1.699056	−0.0037
	0.029684	0.048184	1.581497	0.016745	0.037808	1.581671
Subim ($l_f = 5$ voxels)	5.027286	−2.06213	−0.1151569	5.047299	−2.06356	−0.07676
	−1.968577	4.084249	−0.648477	−1.99923	4.087375	−0.66427
	−0.266148	−0.559289	3.872259	−0.30344	−0.57343	3.870076
Subim ($l_f = 30$ voxels)	13.020648	−3.733625	−1.085037	13.07684	−3.79502	−1.01717
	−3.850933	11.15109	−2.3809	−3.955	11.17836	−2.4345
	−1.486225	−2.33157	11.546347	−1.58909	−2.36035	11.5474

done on the scheme at Fig. 2) for observed flow patterns. Again, we draw attention to the differences between the CW and Per cases which highlight the distinction between the absence and presence of transversal flow. The Free case shows inflow-outflow pathways on the walls which divide the domain into a central zone (with flow in the direction of the gradient) and convective-like zones along the walls which significantly accelerate the ensemble flow velocities.

The Sym case is better explained using eigenvectors instead of flow velocity vectors, as shown in Fig. 8(e). Each original subvolume (or a part of the central subvolume) has its own permeability eigenvector. By mirroring the subvolume geometries, their directions cancel out all transversal flow and immediately result in zero off-diagonal permeability tensor terms. The Trans and Subim cases have similar patterns to that of the Per case, as discussed above, while the magnitude
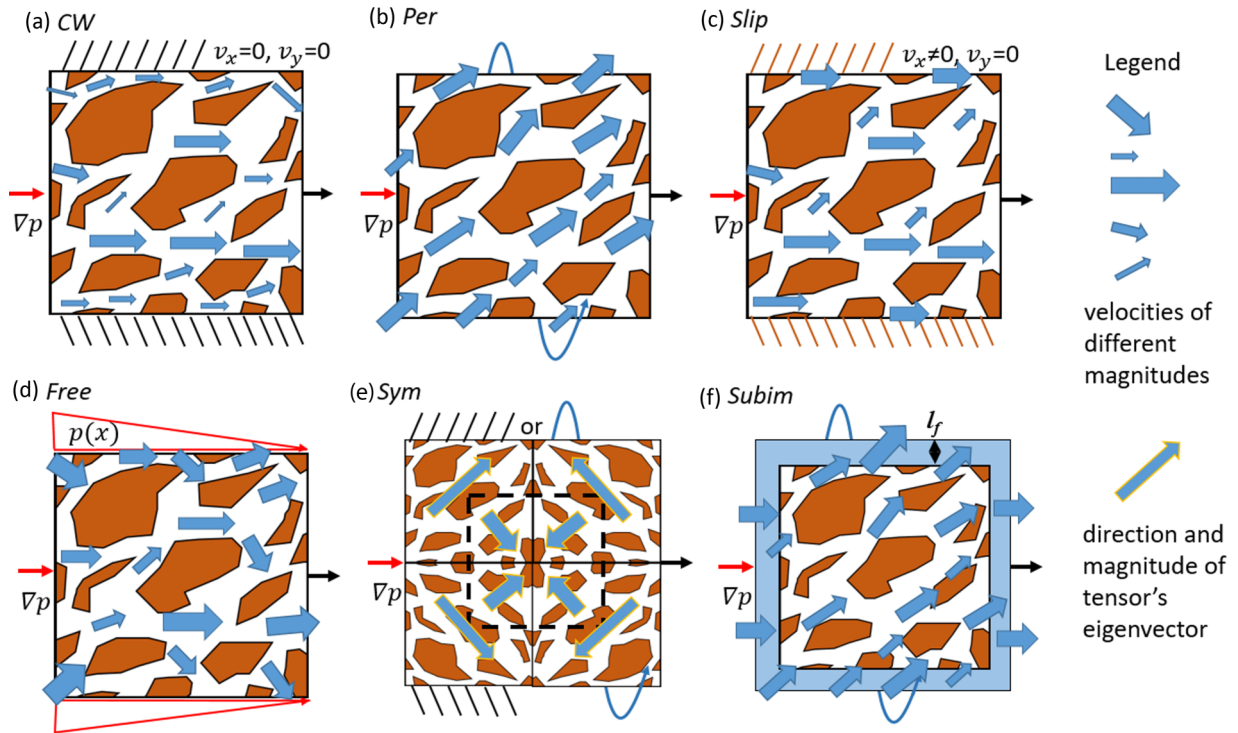
FIG. 8. General scheme of the flow patterns observed in the soil and shale reconstructed samples based on the following boundary conditions: (a) CW, (b) Per, (c) Slip, (d) Free, (e) Sym, and (f) Subim. This scheme does not follow soil and shale sample flow lines closely but provides the general difference between those under the conditions investigated.

increment for Subim depends on the l_f values. Notably, only Per and Subim BCs produce flow patterns that we expect to happen in real conditions when porous rock is part of the larger matrix domain [Fig. 2(a)].

E. General discussion and outlook

The usage of 3D stochastic reconstruction technique allowed us to utilize periodic flow boundary condition and physically reproduce real flow patterns in the rock massif. Based on all results of our pore-scale modeling study (mainly Tables III and IV and Figs. 6–8) we argue that the Per boundary condition is the most suitable to simulate tensorial flow properties. The immersion of the studied sample into homogeneous media such as fluid or continuum-scale representation [18] preserves the tensors orientation but may change the magnitude. The way to preserve the magnitude is to encapsulate the sample into its statistically similar geometrically periodical shell with the same permeability tensor and stochastic reconstructions providing a readily available solution.

Now that we have observed significant differences between different BCs and established the correct one, it is important to show that these differences are not due limited size effects. Conventionally this is done by showing that the sample is representative in terms of a studied physical property. To perform conventional permeability REV analysis we calculate a full tensor for cubical subdomains with widths of 40–160 voxels around the center of the full-sized sample. For each simulation we calculate eigenvalues and plot them against the domain size. If with increasing domain size permeability eigenvalues converge to stable values, then this would indicate reaching REV. The results of such an analysis for shale and soil samples are shown in Fig. 9. To further facilitate the comparison between different subdomains we included visualizations of the full permeability tensor similar to those in Fig. 6 for each subdomain size. Our analysis clearly indicates that both shale and soil samples are permeability REVs. The shale sample's flow property converges around 120 voxels, while the soil sample hits the plateau around 110 voxels—both in very good agreement (decay of L_2) with statistical measures as shown in Fig. 4. While this is not necessarily true for many real porous media samples where different physical properties may have very different REV sizes, such excellent agreement between morphological and permeability REVs for both samples is most likely due to a correlation functions-based stochastic reconstruction methodology that insures statistical homogeneity of the reconstruction if morphological REV is reached.

The study as described here is not without limits, which hindered carefully explaining all processes related to pore-scale single-phase flow and its upscaling to a tensorial permeability. In particular, we studied stochastic reconstructions of shale and soil samples of limited size (160^3 voxels) with both having somewhat similar structure by design. The numerical tools we used to solve Stokes's equation put a limit on inlet-outlet boundary conditions we utilized for simulations. However, insights are provided below on how to circumvent such issues in future.

The samples of porous media studied here, namely stochastic reconstructions of shale and soil, while clearly
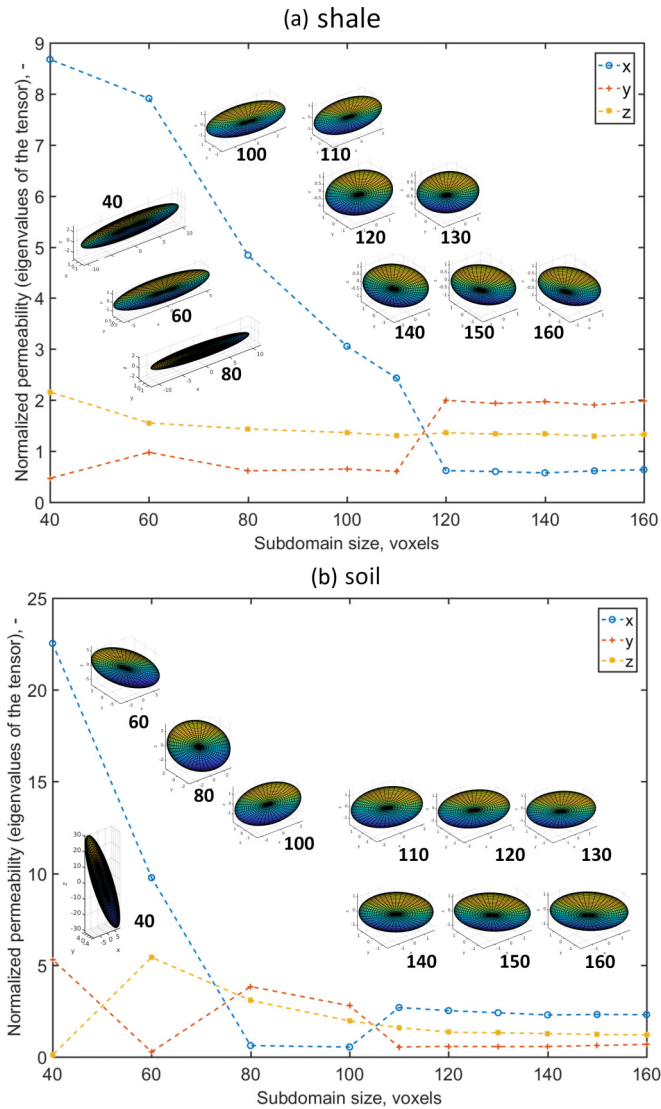
FIG. 9. Permeability REV analysis for (a) shale and (b) soil samples. The analysis is based on permeability tensor evaluation (based on Per boundary conditions) in terms of eigenvectors along the x, y, and z major directions (y axis) plotted versus increasing volume of the cubical domain (x axis). In addition to eigenvalues, a visual representation of the full permeability tensor is shown for each domain size to facilitate the comparison.

demonstrating REV permeability behavior (Fig. 9), had a somewhat limited volume of 160^3 voxels, which was mainly due to limitations in available computational resources. For larger samples, the effects of the boundary conditions could be less pronounced as the volume grows faster than the boundary area with increasing cube width. Some effects of the increasing volume can be seen from the Trans (CW) case for the full domains of 320^3 voxels (Tables III and IV)—with an 8 times increase in volume Trans (CW) the permeability tensor magnitude grows by approximately 9.75 and 12.49% compared to CW for shale and soil (as computed using eigenvalues), respectively. The fact that permeabilities of full Trans (CW) cases for both porous media types were higher than CW clearly supports the idea that transversal flow

is crucial for permeability tensor evaluation. It is possible to investigate the influence of volume size further in future studies by considering larger samples. On the other hand, using smaller samples as used here allowed for highlighting the differences between different boundary conditions.

The size of the modeling domain definitely affects the influence of different BCs. Strictly speaking, the inaccuracies introduced by, for example, CW or Free, will diminish to practically zero in the limit of infinite domain size. From the practical point of view it seems to be possible to find a size with inaccuracies not exceeding some threshold, say, error of 5% in terms of tensor eigenvalues. However, we argue that a possibility to find such a volume may be hindered by the inhomogeneity of the sample under study. While it is possible to increase the volume of stochastic reconstruction and still obtain the same permeability tensor due to statistical stationarity, this is hardly true for real porous media such as rocks and soils that have distinct layers, multiscale structure, or genetic horizons—all with their limited sizes or correlation lengths. In such complex porous media, for example, carbonates, it is sometimes even not possible to establish a permeability REV on the pore scale [16,61]. Such examples seems to be the norm rather than the exception for real rocks and soils, thus diminishing the scientific and practical value of the conventional REV upscaling approach. For these reasons we speculate that the methodology to evaluate tensorial properties using the Per BC will be invaluable for the majority of real upscaling cases where an increase in the simulation domain will average out the effects of local imhomogeneities (e.g., Ref. [62]).

Both 3D stochastic reconstructions used to calculate tensorial permeabilities are somewhat similar by design: They are both statistically homogeneous and highly anisotropic media. The anisotropy in the diagonal direction was intended to produce permeability tensors with significant off-diagonal terms. While it was exactly what was needed to magnify the manifestation of the tensorial permeability calculation, two factors were left out of consideration. First, we included no sample with a zero off-diagonal permeability term, for which the influence of the Per boundary condition is known to be less pronounced and similar to that of the Slip BC [33,47]. Second, only statistically homogeneous structures were considered, while nonstationary porous media are ubiquitous in nature. Both topics are of utmost importance for upscaling and experimental flow measurements (see discussion below), but well beyond the scope of this paper.

Both CW and Slip BCs produced transversal pressure gradients, as opposed to the applied gradient in a single direction only (by creating pressure difference between inlet and outlet only), while Per-Free-Subim BCs maintained pressure gradient in the applied direction. From the viewpoint of the Eq. (7) it does not matter if transversal pressure gradients are present, e.g., one can compute tensorial properties by applying pressure gradient in nonorthogonal directions. Yet, from the theoretical point of view, the presence of transversal components if the gradient is applied in a given direction is unphysical. Here we can speculate that both Dirichlet (first type or pressure gradient used in this work) and Neumann (second type or flux) are an incorrect choice to simulate a case as shown in Fig. 2(a), as the resulting pressure gradient

may be different from that intended to be applied. Thus, immersing the simulation domain into an external gravity field or creating a body force as done in LBM simulations [15] seems to be a better alternative. Such pressure-gradient behavior in our simulations actually could be one reason for nonsymmetry of the tensorial permeability, as velocity fields are not normalized by local pressure perturbations. The symmetrization of tensors using either Eq. (9) or Eq. (10) does not seem to be a physically adequate approach, but if symmetrization is unavoidable, for example, to provide input data for continuum-scale model, hten Eq. (9) is a better option. We observed all Sym BC simulations to produce a symmetrical tensor (all pressure gradients are located at subdomain boundaries); this suggests that artificial symmetrization is indeed unphysical and proper pressure gradient application is a correct solution of the nonsymmetry issue.

The results obtained clearly indicate that numerous classical boundary conditions, such as CW, Free, and Sym, are unphysical to obtain flow tensorial properties simulated on the pore level. However, application of all BCs on the continuum- (or Darcian) scale understudy is still ongoing and requires thorough investigation. The Free boundary condition is popular for fractured porous media equivalent permeability tensor evaluation [48], but as observed in this study spurious flow patterns cause erroneous tensor values. To what extent this problem will arise in large-scale problems, especially with heterogeneous matrix in between the fractures, is impossible to predict without detailed simulations. The leap from the pore scale to continuum scale, or upscaling, is a crucial step necessary for adequate parametrization of large-scale hydrodynamic models and is usually performed using laboratory measurements on the rock and soil cores. If not aligned along the permeability eigenvector [63], then conventional permeameter types of laboratory investigations on the core sample may result in severe errors in permeability magnitude and orientation.

IV. SUMMARY

Pore-scale simulations of single-phase flow within 3D geometrically periodical porous media obtained using stochastic reconstructions from real soil and shale images allowed for the implementation of periodic flow boundary conditions. Unlike numerous classical boundary conditions utilized to compute permeability on the pore scale, namely closed walls (parallel to applied pressure gradient), linear pressure on the walls, translation, and symmetry, the periodic flow boundary condition reproduces the physical flow patterns within porous media. Reproducing such flow patterns is important for upscaling of flow properties from pore to continuum scale. Our results strongly suggest that correct upscaling is not possible without considering tensorial flow properties.

We anticipate that the description of other physical properties relevant to porous media and materials in general, for example, mechanical properties, transport properties (dispersion), electricity and heat conduction, and related properties, may benefit from applying periodic boundary conditions. In particular, we believe that multiphase flow properties (e.g., relative permeabilities) should be computed in a manner demonstrated in this study. Stochastic reconstructions allow for the creation of statistically identical 3D replicas with periodic geometries. A variety of existing techniques could be used for this purpose: correlation functions-based methods [[30,39,41,44],[64,65]], multiple-point statistics [66–68] and related techniques [69–71]. A more general solution applicable to experimentally obtained images is currently under development.

[1] M. Sahimi, *Flow and Transport in Porous Media and Fractured Rock: From Classical Methods to Modern Approaches* (John Wiley & Sons, New York, 2011).

[2] M. J. Blunt, *Multiphase Flow in Permeable Media: A Pore-Scale Perspective* (Cambridge University Press, Cambridge, 2017).

[3] J. R. A. Godinho, K. M. Gerke,, A. G. Stack, and P. D. Lee, Sci. Rep. **6**, 33086 (2016).

[4] K. M. Gerke, R. C. Sidle, and D. Mallants, Hydrol. Process. **29**, 4562 (2015).

[5] H. H. Gerke, J. Plant Nutr. Soil Sci. **169**, 382 (2006).

[6] T. Tranter, J. Gostick, A. Burns, and W. Gale, Transp. Porous Media **121**, 597 (2018).

[7] Q. Xiong, C. Joseph, K. Schmeide, and A. P. Jivkov, Phys. Chem. Chem. Phys. **17**, 30577 (2015).

[8] D. Mallants, J. Marivoet, and X. Sillen, J. Nucl. Mater. **298**, 125 (2001).

[9] A. Derossi, K. M. Gerke, M. V. Karsanina, B. Nicolai, P. Verboven, and C. Severini, J. Food Eng. **241**, 116 (2019).

[10] G. E. Pickup, K. S. Sorbie *et al.*, SPE J. **1**, 369 (1996).

[11] P. Renard and G. De Marsily, Adv. Water Resour. **20**, 253 (1997).

[12] M. Bagheri, A. Settari *et al.*, J. Can. Pet. Technol. **46** (2007).

[13] P. Renard, A. Genty, and F. Stauffer, J. Geophys. Res.: Solid Earth **106**, 26443 (2001).

[14] C. Manwart, U. Aaltosalmi, A. Koponen, R. Hilfer, and J. Timonen, Phys. Rev. E **66**, 016702 (2002).

[15] S. A. Galindo-Torres, A. Scheuermann, and L. Li, Phys. Rev. E **86**, 046306 (2012).

[16] K. M. Gerke, R. V. Vasilyev, S. Khirevich, D. Collins, M. V. Karsanina, T. O. Sizonenko, D. V. Korost, S. Lamontagne, and D. Mallants, Comput. Geosci. **114**, 41 (2018).

[17] A. Q. Raeini, M. J. Blunt, and B. Bijeljic, J. Comput. Phys. **231**, 5653 (2012).

[18] R. Guibert, P. Horgue, G. Debenest, and M. Quintard, Math. Geosci. **48**, 329 (2016).

[19] T. W. Thibodeaux, Q. Sheng, and K. E. Thompson, Ind. Eng. Chem. Res. **54**, 4474 (2015).

[20] D. Wildenschild, C. Vaz, M. Rivers, D. Rikard, and B. Christensen, J. Hydrol. **267**, 285 (2002).

[21] V. Cnudde and M. N. Boone, Earth-Sci. Rev. **123**, 1 (2013).

[22] K. Gerke, E. Skvortsova, and D. Korost, Euras. Soil Sci. **45**, 700 (2012).

[23] K. M. Gerke, M. V. Karsanina, and D. Mallants, Sci. Rep. **5**, 15880 (2015).

[24] K. Gerke, M. Karsanina, T. Sizonenko, X. Miao, D. Gafurova, and D. Korost, in *Proceedings of the SPE Russian Petroleum Technology Conference*, SPE 187874 (SPE, Moscow, 2017).

[25] M. V. Karsanina, K. M. Gerke, E. B. Skvortsova, A. L. Ivanov, and D. Mallants, Geoderma **314**, 138 (2018).

[26] P. Adler, C. Jacquin, and J. Quiblier, Int. J. Multiphase Flow **16**, 691 (1990).

[27] C. L. Y. Yeong and S. Torquato, Phys. Rev. E **57**, 495 (1998).

[28] K. M. Gerke, M. V. Karsanina, and E. B. Skvortsova, Euras. Soil Sci. **45**, 861 (2012).

[29] A. Derossi, C. Severini, and T. De Pilli, J. Food Eng. **142**, 9 (2014).

[30] M. V. Karsanina, K. M. Gerke, E. B. Skvortsova, and D. Mallants, PLoS One **10**, e0126515 (2015).

[31] M. Karsanina, K. Gerke, R. Vasilyev, and D. Korost, Math. Model. Comput. Simul. **27**, 50 (2015).

[32] Y. Xu, S. Chen, P.-E. Chen, W. Xu, and Y. Jiao, Phys. Rev. E **96**, 043301 (2017).

[33] K. M. Gerke and M. V. Karsanina, Europhys. Lett. **111**, 56002 (2015).

[34] S. Chen, A. Kirubanandham, N. Chawla, and Y. Jiao, Metall. Mater. Trans. A **47**, 1440 (2016).

[35] P. Tahmasebi, Fuel **217**, 218 (2018).

[36] G. Mariethoz, P. Renard, and J. Straubhaar, Water Resour. Res. **46**, W11536 (2010).

[37] P. Tahmasebi, F. Javadpour, M. Sahimi, and M. Piri, Adv. Water Resour. **89**, 91 (2016).

[38] D. Gilyazetdinova and D. Korost, Mosc. Univer. Geol. Bull. **71**, 81 (2016).

[39] M. V. Karsanina and K. M. Gerke, Phys. Rev. Lett. **121**, 265501 (2018).

[40] S. Torquato, *Random Heterogeneous Materials: Microstructure and Macroscopic Properties* (Springer-Verlag, New York, 2002), p. 703.

[41] K. M. Gerke, M. V. Karsanina, R. V. Vasilyev, and D. Mallants, Europhys. Lett. **106**, 66002 (2014).

[42] S. Kirkpatrick, C. D. Gelatt, Jr., and M. P. Vecchi, Science **220**, 671 (1983).

[43] N. Metropolis, A. W. Rosenbluth, M. N. Rosenbluth, A. H. Teller, and E. Teller, J. Chem. Phys. **21**, 1087 (1953).

[44] P. Čapek, V. Hejtmánek, J. Kolafa, and L. Brabec, Transp. Porous Media **88**, 87 (2011).

[45] M. Veselý, T. Bultreys, M. Peksa, J. Lang, V. Cnudde, L. Van Hoorebeke, M. Kočiřík, V. Hejtmánek, O. Šolcová, K. Soukup, K. Gerke, F. Stallmach, and P. Čapek, Transp. Porous Media **110**, 81 (2015).

[46] http://iso2mesh.sourceforge.net/cgi-bin/index.cgi.

[47] P. Eichheimer, M. Thielmann, A. Popov, G. J. Golabek, W. Fujita, M. O. Kottwitz, and B. J. P. Kaus, Solid Earth **10**, 1717 (2019).

[48] M. Oda, Geotechnique **35**, 483 (1985).

[49] S. Whitaker, Transp. Porous Media **1**, 3 (1986).

[50] A. Liakopoulos, Hydrol. Sci. J. **10**, 41 (1965).

[51] Y. Jobic, P. Kumar, F. Topin, and R. Occelli, Int. J. Multiphase Flow **110**, 198 (2019).

[52] L. J. Durlofsky, Water Resour. Res. **27**, 699 (1991).

[53] S. Azizmohammadi and S. K. Matthäi, Water Resour. Res. **53**, 8041 (2017).

[54] P. Čapek, V. Hejtmánek, L. Brabec, A. Zikánová, and M. Kočiřík, Transp. Porous Media **76**, 179 (2009).

[55] R. Guibert, M. Nazarova, P. Horgue, G. Hamon, P. Creux, and G. Debenest, Transp. Porous Media **107**, 641 (2015).

[56] S. Khirevich and T. W. Patzek, Phys. Fluids **30**, 093604 (2018).

[57] J. Bear, *Modelling Phenomena of Flow and Transport in Porous Media* (Springer Nature, Cham, 2018), p. 742.

[58] J. Bear, J. Geophys. Res. **66**, 1185 (1961).

[59] J. Salles, J. Thovert, R. Delannay, L. Prevors, J. Auriault, and P. M. Adler, Phys. Fluids A **5**, 2348 (1993).

[60] P. S. Lang, A. Paluszny, and R. W. Zimmerman, J. Geophys. Res.: Solid Earth **119**, 6288 (2014).

[61] P. Mostaghimi, M. J. Blunt, and B. Bijeljic, Math. Geosci. **45**, 103 (2013).

[62] D. Mallants, B. P. Mohanty, A. Vervoort, and J. Feyen, Soil Technol. **10**, 115 (1997).

[63] K. Gerke, M. Karsanina, A. Khomyak, B. Darmaev, and D. Korost, in *Proceedings of the SPE Russian Petroleum Technology Conference* (SPE, Moscow, 2018).

[64] Y. Jiao, F. H. Stillinger, and S. Torquato, Proc. Natl. Acad. Sci. USA **106**, 17634 (2009).

[65] Y. Jiao and N. Chawla, J. Appl. Phys. **115**, 093511 (2014).

[66] P. Tahmasebi and M. Sahimi, Phys. Rev. E **85**, 066709 (2012).

[67] P. Tahmasebi and M. Sahimi, Phys. Rev. Lett. **110**, 078002 (2013).

[68] Q. Chen, G. Mariethoz, G. Liu, A. Comunian, and X. Ma, Hydrol. Earth Syst. Sci. **22**, 6547 (2018).

[69] L. Mosser, O. Dubrule, and M. J. Blunt, Phys. Rev. E **96**, 043309 (2017).

[70] Y. Li, Q. Teng, X. He, C. Ren, H. Chen, and J. Feng, Phys. Rev. E **99**, 062134 (2019).

[71] J. Feng, X. He, Q. Teng, C. Ren, H. Chen, and Y. Li, Phys. Rev. E **100**, 033308 (2019).